Asian Journal of Chemistry; Vol. 35, No. 2 (2023), 345-351

ASIAN JOURNAL OF CHEMISTRY

https://doi.org/10.14233/ajchem.2023.23484

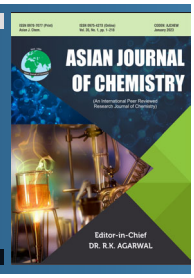

Precipitation Method and Sonication Technique for Advanced Superiority of Nanospherical $BiFe_2O_3$ and its Multi-Applications

R. JAYASAKTHI and G. SIVAKUMAR*

PG & Research Department of Physics, Annamalai University, Annamalainagar-608002, India

*Corresponding author: E-mail: gsk_cisl@yahoo.com

Received: 15 September 2022; *Accepted*: 7 November 2022; *Published online*: 30 January 2023; AJC-21115

In this work, a modified $BiFe_2O_3$ nanomaterial was prepared using a combination of co-precipitation and sonication methods. High-resolution scanning electron microscopy (HRSEM) results revealed a nanospherical shaped structure. The energy dispersive X-ray analysis (EDX) analysis confirmed that Bi, Fe and O are present in the $BiFe_2O_3$ nanomaterial. The photoluminescence analysis also confirmed the presence of bismuth in the $BiFe_2O_3$ nanomaterial. The recombination of electron-hole pairs in Fe_2O_3 transpires when the electrons and holes were transferred between Bi and Fe_2O_3 nanomaterials. The UV-Vis DRS analysis revealed that the nanomaterial decrease band gap energy and increased the photoenergy. The modified $BiFe_2O_3$ was successfully used as multi-functional materials, such as a photocatalytic material for the photodegradation of Rhodamine B and Rhodamine 6G dyes, antibacterial agent and as improved dye sensitized solar cells (DSSCS).

Keywords: $BiFe_2O_3$ nanomaterial, Photocatalytic activity, Antibacterial activity, Rhodamine B, Rhodamine 6G, DSSCs.

INTRODUCTION

Large amounts of attention are focused on the perovskite materials with the general formula ABX_3 or ABO_3, where 'A' and 'B' are two cations of different sizes and 'X' is an anion that bonds to both, due to their many desirable properties and found its applicability in various fields like electrochemical, waste-water treatment, magnetite, catalysis, biomedicines, *etc*. [1-4]. In addition to study the chemical degradation, perovskite structures' electrochemically driven ion evolution behaviours have gained a lot of interest because of their one-of-a-kind features and applications [5-7].

Recent advances in bismuth ferrite nanoclusters seem to be a good semiconductor material for eleminating a wide range of dyes since they can handle a wide range of frequencies, absorb a lot of visible light and are stable. When thin sheets of bismuth ferrite are changed, there is lots of the improvement in the properties happens [8-10]. At the nanoscale, bismuth ferrite materials exhibit new physical properties, which are different from what they possess in bulk or as a thin film [11-14].

The synthetic method has a significant impact on the chemical, morphological and the optical properties of perovskite materials, as is well known. The crystal structure and the shape of the samples are also altered by the different synthetic routes [15]. Early in 1967, Achenbach *et al*. [16] reported a single phase polycrystalline BFO *via* solid-state reaction of BiO and FeO at < 700 ºC. However, this method has some drawbacks, including a high reaction temperature, big particle size and the existence of contaminants. Alternatively, new methods *e.g*. chemical coprecipitation [17,18], hydrothermal [19], solvothermal [20], sonochemical [21], microemulsion [22], polyacrylamide gel [23], ferrioxalate [24], simple sol-gel [25], combustion synthesis [26], molten salt [27], tartaric acid assisted gel strategy [28], polymeric precursor [29] and mechanochemical synthetic route [30] are nowadays used commonly for the synthesis of bismuth ferrite nanopowders.

In this study, a broad $BiFe_2O_3$ nanomaterial was prepared using a combination of co-precipitation and sonication methods approach for producing consistent $BiFe_2O$ nanomaterial. The prepared nanomaterial were characterized from HR-SEM, EDX, HR-TEM, XRD, photoluminescence spectroscopy and UV-Vis DRS analysis. Moreover, modified $BiFe_2O_3$ was successfully employed as an antibacterial agent, photocatalytic photodegradation of Rhodamine B and Rhodamine 6G dyes and enhanced dye sensitized solar cells (DSSCS).

EXPERIMENTAL

Ammonia solution, conc. nitric acid, bismuth nitrate pentahydrate [$Bi(NO_3)_3{\cdot}5H_2O$], ferric chloride hexahydrate [($FeCl_3{\cdot}6H_2O$)], FTO-plate, Rhodamine B and Rhodamine 6G dyes were acquired from Sigma-Aldrich and used as received. Anthocynin dye was generated from the natural flower extract solution, ethanol solution and used as such. All the glasswares were acid washed before being completely washed with distilled water. Deionized water and ordinary water were used as controls throughout the experiment, with deionized water being used in the degradation processes.

Synthesis of Bi doped Fe_2O_3: A simple co-precipitation process and sonication technique were used to prepare bismuth doped Fe_2O_3 nanomaterial. Ferric chloride hexahydrate (3 g) was dissolved in 100 mL of deionized water (solution A) and $Bi(NO_3)_3{\cdot}5H_2O$ (0.1 M) was dissolved in 50 mL of deionized water (solution B). Under vigorous stirring, solution B was mixed into solution A dropwise manner. This precursor mixture was agitated at room temperature for 30 min before being adjusted to pH = 9 with ammonia solution. The resulting solution was again agitated for 3 h before being ultrasonicated for 40 min. The resulting precipitate was filtered and rinsed with distilled water followed by ethanol. The precipitate was then collected, dried for 15 h at 100 ºC in an oven and then calcined in a muffle furnace at 500 ºC for 4 h.

Characterization: The structural characterization of the deposited films was reported using Shimadzu-6000 (monochromatic Cu*K*α radiation, λ = 1.5406 Å). The XRD patterns were identified in two intervals of 10º to 90º with 0.05º increments. The HR-SEM was used to investigate the surface morphology (JEOL-JES-1600). At 25 ºC, the EDX assessment trials were carried out on an FEI Quanta FEG 200 apparatus equipped with an EDX analyzer with transmissions with high resolution. The HR-TEM images were captured using a JEOL-JEM-2010 UHR system with a lattice image resolution of 0.14 nm and a 200 kV acceleration voltage. A Perkin-Elmer LS 55 fluorescence spectrometer was used to capture photoluminescence (PL) spectra at room temperature, while a Hitachi-U-2001 spectrophotometer was used to measure ultraviolet and visible (UV-Vis) absorbance spectra throughout a wavelength range of 800-200 nm using a quartz cell with a 10 mm optical path length. The photovoltaic evaluation of the prepared nanomaterial was done by recording the photocurrent voltage (I-V) curve under Ampere metres (A.M.) at 1.5 (100 Mw/cm^2) light.

RESULTS AND DISCUSSION

Surface topography: The micrograph of calcined 500 ºC prepared Bi doped Fe_2O_3 nanomaterial consisted of well-defined nanospherical like structure (Fig. 1a), which also cleary exhibited homogeneous uniform distribution, thus, the surface morphology has high efficiency of photocatalytic activity. Fig. 1b shows the clearly sharp high density of Fe and O, the decreasing density of Bi and the totally homogenous circulation of Bi, Fe and O indicates the purity of the nanomaterial, when analyzed with energy dispersive X-ray spectroscopy (EDX) were carried out.

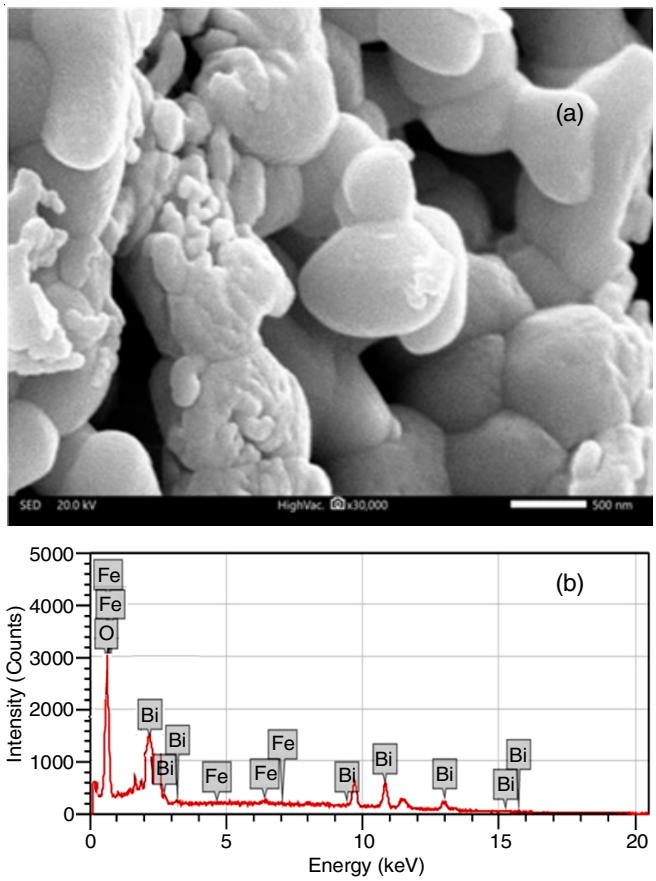

Fig. 1. SEM analysis of (a) SEM image $BiFe_2O_3$ nanomaterial and (b) EDS analysis

The prepared $BiFe_2O_3$ nanomaterial was consisted of well-defined nanospherical like structure as exhibited from Fig. 2a, whereas Fig. 2b showed the number of bright rings, which correspond to the polycrystalline nature. Fig. 2c represented a 3D structured by selecting and highlighting electron area, whereas Fig. 2d shows a average particle angle size range distribution 28 nm and has average particle maximum size range distribution of 51 nm, which was calculated using Image J Viewer software.

XRD studies: The prepared $BiFe_2O_3$ nanomaterial annealed at 500 ºC for 4 h revealed the sharp peaks presents its high crystallinity structure. The prepared bismuth doped Fe_2O_3 exhibit the XRD peaks at 22.5º, 24.8º, 30.1º, 32.1º, 33.6º, 36.2º, 40.4º, 47.2º, 52.0º and 56.1º are indexed to the (003), (101), (110) planes (JCPDS no. 36-1451, 44-1246 and 79-0206) [19, 20], moreover the additional small peaks at 28º and 32º conformed that bismuth is well doped onto Fe_2O_3 [21-23] (Fig. 3a-b). The crystal structures of Fe_2O_3 and $BiFe_2O_3$ nanomaterials were FCC and its particle size were found to be 21 and 16 nm, respectively as calculated from the Debye-Scherrer's equation.

Photoluminescence (PL) studies: Fig. 4 shows the PL spectra of Fe_2O_3 and as-prepared $BiFe_2O_3$ nanomaterial at the excitation wavelength of λ = 320 nm. For both materials, the emissions at 330, 360, 380, 420, 440 and 540 nm are same and although different intensities was obtained. The Fe_2O_3 nanomaterial was high at 500 nm, while in case of $BiFe_2O_3$ nanomaterial, a low intensity was observed, which demonstrated the

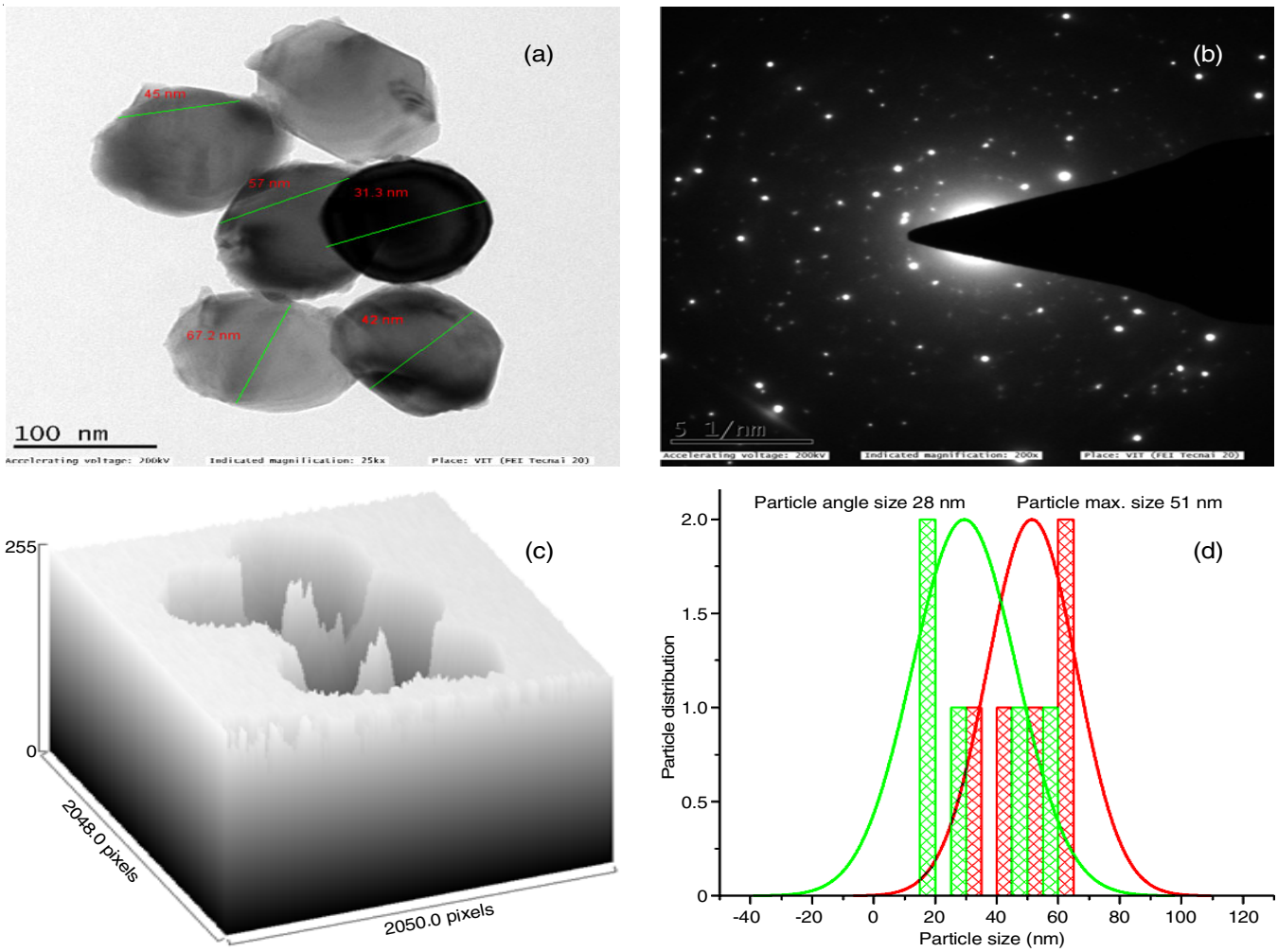

Fig. 2. HR-TEM micrographs; (a) image of $BiFe_2O_3$, (b) SAED pattern, (c) image profile 3D structure and (d) average particle angle size 28 and particle max size 51 nm by selected particle length area highlighted in HR-TEM image (a)

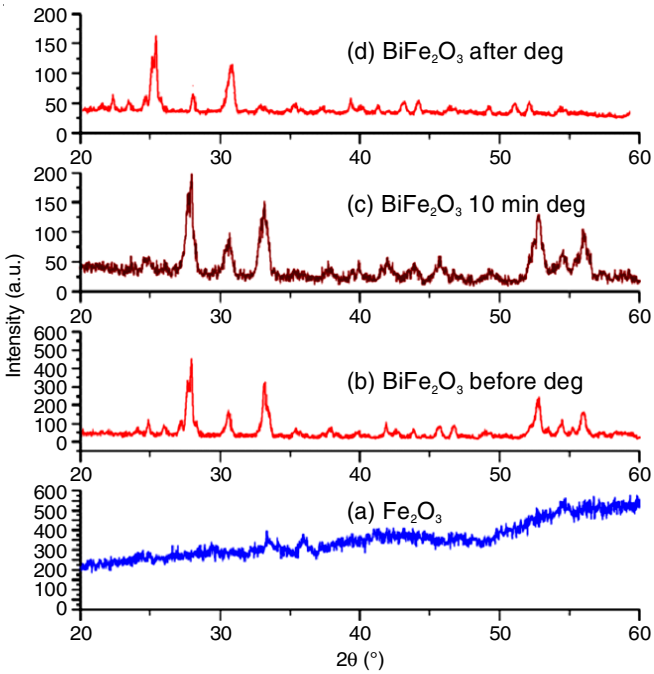

Fig. 3. XRD analysis of (a) Fe_2O_3, (b) $BiFe_2O_3$, (c) $BiFe_2O_3$ after 10 min degradation and (d) $BiFe_2O_3$ after deg. nanomaterial

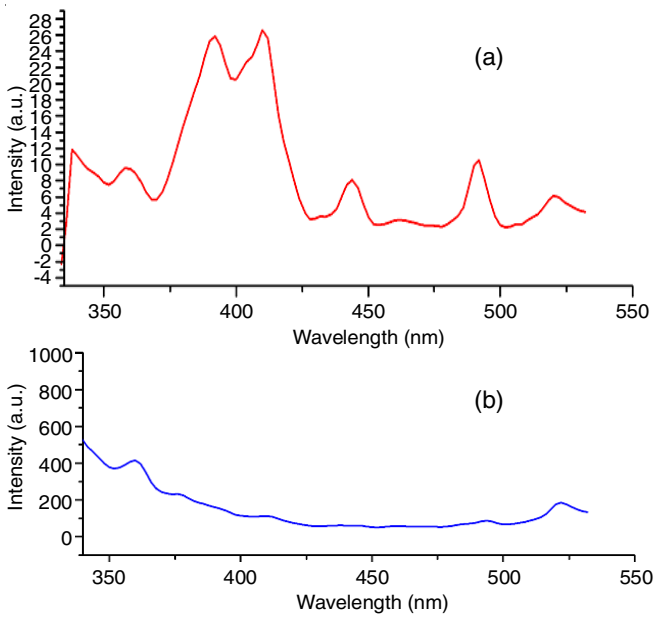

Fig. 4. PL spectra of (a) Fe_2O_3 and (b) $BiFe_2O_3$ nanomaterial

extending life-times of electrons and holes resulting in the enhanced optical, electrical and microbiological performances [26,27].

UV-Vis-DRS studies: The UV-Vis-DRS analysis of the synthesized Fe_2O_3 and $BiFe_2O_3$ nanomaterials revealed the UV and visible absorption in the 200-800 nm range. The Kubelka-Munk (KM) function was used to transform the DRS spectra (R). The direct band gap of the synthesized material has been determined from the Tauc plot using UV-Vis-DRS spectra of synthesized Fe_2O_3 and $BiFe_2O_3$ nanomaterial. A blue shift observed in Fe_2O_3 nanomaterial was due to the size effect (Fig. 5). The band gap energies of Fe_2O_3 and $BiFe_2O_3$ nanomaterials were found to be 2.3 and 2.05 eV, respectively. These findings suggested that doping nanomaterials with low band gap energy cause higher light absorption [31-34].

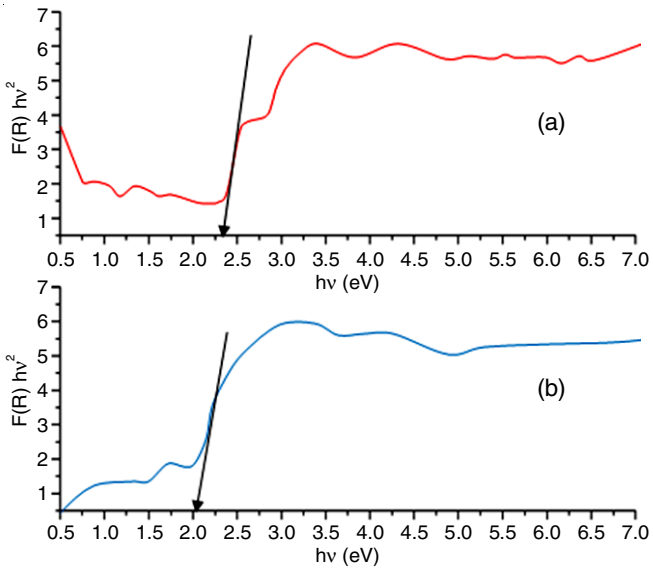

Fig. 5. UV-Vis DRS of plot of transferred Kubelka-Munk *vs.* energy of light absorbed of (a) Fe_2O_3 and (b) $BiFe_2O_3$ nanomaterial

Photocatalytic activity: The photocatalytic degradation of prepared Fe_2O_3 and $BiFe_2O_3$ nanomaterial on rhodamine B (Rh B) and rhodamine 6G (Rh 6G) dyes were exposed to UV light at 365 nm for 50 min at the span of every 10 min. The effeciency degradation of dye under different conditions *e.g.* (a) dye + UV + No catalyst; (b) dye + $BiFe_2O_3$ + dark; (c) dye + Fe_2O_3 + UV and (d) dye + $BiFe_2O_3$ + UV analysis results in the degradation of rhodamine 6G dye (0, 1, 2, 3, 5.5 and 8%), (0, 2, 4, 6, 9 and 13%), (0, 8, 15, 28, 39 and 54%) and (0, 11, 24, 50, 78 and 96%), respectively (Fig. 6a-d). Under the same concentration and dosage catalyst amount, the photocataylic degradation efficiency is very high for $BiFe_2O_3$ nanomaterial as compared to undoped Fe_2O_3 nanomaterial. Similarly, the photocatalytic activity for rhodamine B (Rh B), the result patterns are almost same in this case also (Fig. 7a-d). However, the prepared $BiFe_2O_3$ nanomaterial degrade rhodamine 6G (Rh 6G) dye more efficiently than rhodamine B (Rh B) dye.

Influence of parameters

Effect of catalyst loading effect: As can be observed from Fig. 8, the photodegradation efficiency enhanced with an increase in amount up to 0.08 g/50 mL and then significantly decreased with catalyst loadings of 0.04, 0.08 and 0.1 g/50 mL. Thus, catalyst loading of 0.08 g had the best photocatalytic activity.

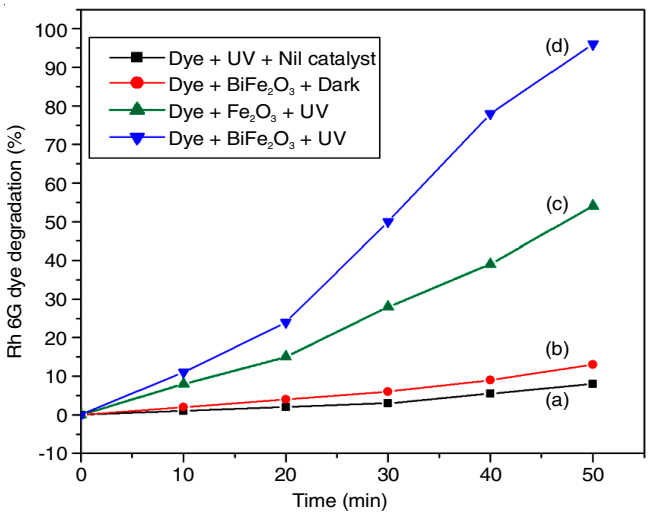

Fig. 6. Effect of photocatalytic efficiency of Rh 6G dye under UV-light irradiation (A) by (a) Dye + UV + Nil catalyst, (b) Dye + $BiFe_2O_3$ + Dark, (c) Dye + Fe_2O_3 + UV and (d) Dye + $BiFe_2O_3$ + UV analysis

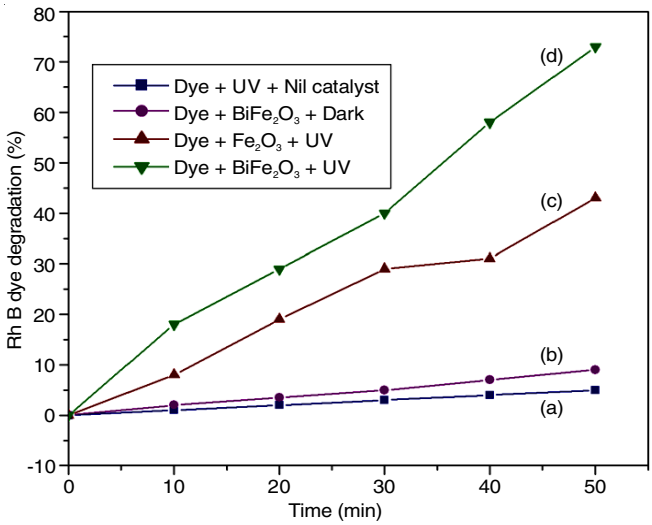

Fig. 7. Effect of photocatalytic efficiency of Rh B dye under UV-light irradiation (A) by (a) Dye + UV + Nil catalyst, (b) Dye + $BiFe_2O_3$ + Dark, (c) Dye + Fe_2O_3 + UV and (d) Dye + $BiFe_2O_3$ + UV analysis

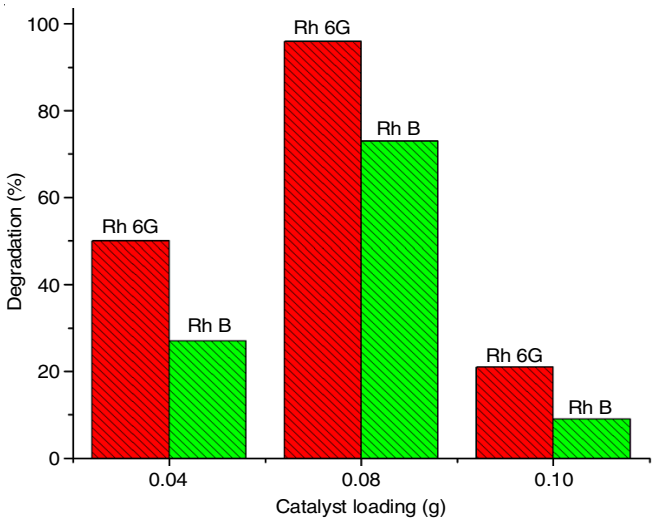

Fig. 8. Effects of catalyst loading (0.04, 0.08 and 0.1 g): Rh 6G and Rh B dye under UV-light irradiation at 365 nm by $BiFe_2O_3$ nanomaterial

however, with further excessive dosage, UV-light diffusion in the particles decreases [35].

Effect of concentrations: Fig. 9 shows that atthe 1×10^{-4} M, Rh 6G and Rh B dyes achieved the maximum degradation efficiency of 96% and 73%, respectively. Upon further increasing the concentration (2×10^{-4} M and 3×10^{-4} M), the percentage of photodegradation activity decreases drastically for both dyes. These results indicated that at high concentration, the catalyst surface area are less available due to the presence of higher dye molecules, which results in the reduction of the photocatalytic activity.

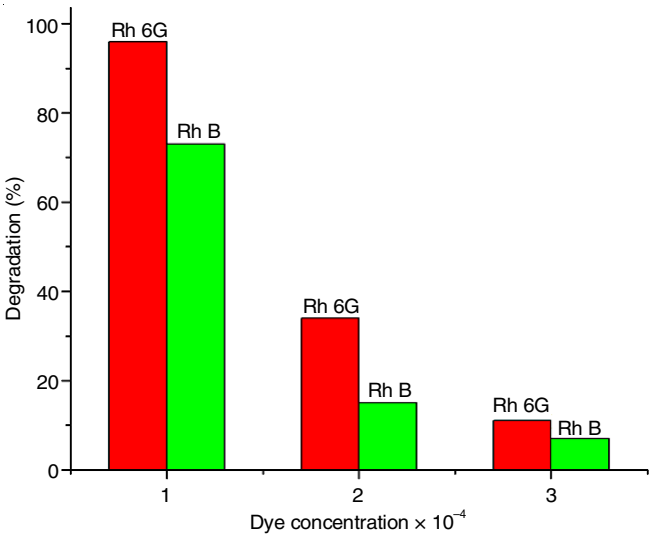

Fig. 9. Effects of different concentrations (1×10^{-4}, 2×10^{-4} and 3×10^{-4} M): Rh 6G and Rh B dye under UV-light irradiation at 365 nm by $BiFe_2O_3$ nanomaterial

Reusability: The photocatalyst's stability and reusability are critical aspects of the catalytic process in the industrial applications. The photocatalytic degradation capabilities of prepared $BiFe_2O_3$ photocatalyst were studied by repeating photocatalytic degradation tests with Rh 6G and Rh B dyes five times. The photocatalysts were extensively washed with water after each cycle and a fresh solution of Rh 6G and Rh B dyes was tested before each photocatalytic run in the photoreactor under UV light. A satisfactory degradation efficiency was achieved within 0-50 min (100, 95, 93, 86 and 86%) as observed in Fig. 10 upto 5 cycles. In comparison to the total dye degradation, catalyst efficiency dropped after the fourth cycle.

Mechanism of photocatalytic efficiency: The mechanism of photocatalytic efficiency as follows:

$$^1\text{Rh 6G dye}_0 + h\nu \longrightarrow \text{Rh 6G dye}_1 \quad (2)$$

$$^1\text{Rh 6G}_1 + \text{ISC} \longrightarrow {}^3\text{Rh 6G dye}_1 \quad (3)$$

$$BiFe_2O_3\,(SC) + h\nu \longrightarrow e^-(CB) + h^+(VB) \quad (4)$$

$$^-OH + h^+ \longrightarrow {}^\bullet OH \quad (5)$$

$$^\bullet OH + {}^3\text{Rh 6G dye}_1 \longrightarrow \text{Leuco Rh B dye} \quad (6)$$

$$\text{Leuco Rh 6G dye} \longrightarrow \text{Products} \quad (7)$$

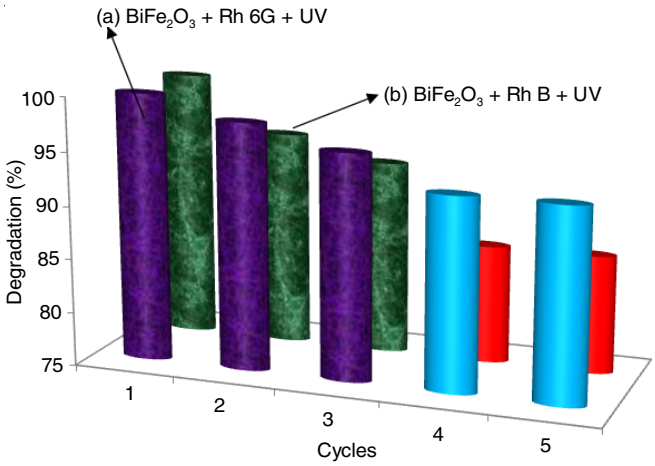

Fig. 10. Reusability of catalyst; Rh 6G and Rh B dye under UV-light irradiation at 365 nm by $BiFe_2O_3$ nanomaterial

Rhodamine 6G (Rh 6G) absorbs photons irradiated from the wavelength and generates an energetic singlet state. It also travels *via* ISC or intersystem crossover to give it an extra established triplet state. This energy was also used by $BiFe_2O_3$ semiconductor or SC to excite its electron from the valence band to the conduction band. A proton can be extracted from ^-OH by a hole (h^+) present in the semiconductor's valence band resulting in the formation of $^\bullet OH$. The Rh 6G dye will be oxidized to its leuco-form by this $^\bullet OH$, which may eventually decay to smallar products. The presence of an $^\bullet OH$ scavenger (2-propanol) significantly reduced the rate of degradation of Rh B dye indicating that $^\bullet OH$ is an active oxidizing species in the degradation of Rh B dye as shown in **Scheme-I** [36].

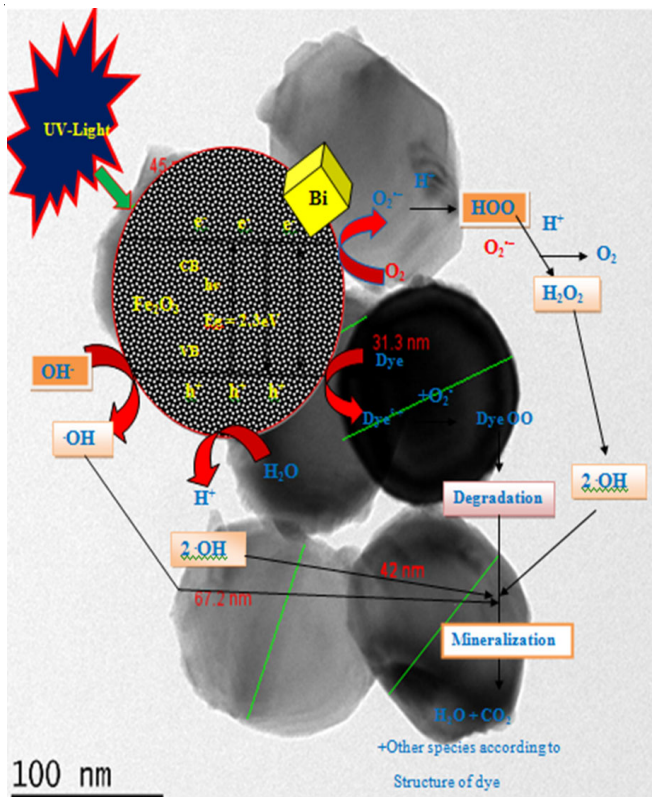

Scheme-I: Schematic representation: Mechanism of $BiFe_2O_3$ nanomaterial

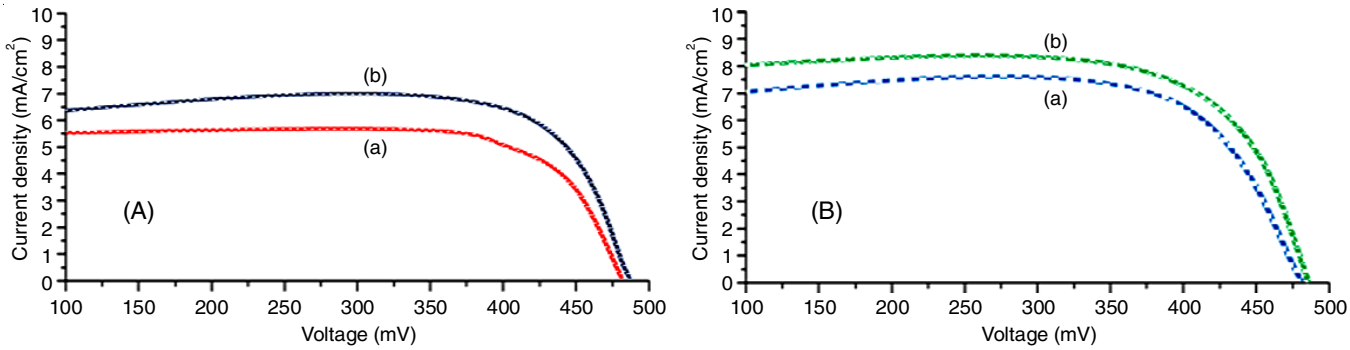

Fig. 11. Current density-voltage (J-V) curves from the DSSC's made-up from fabricated from (A) Rosa[b] flower extract (anthocyanins) dye based sensitized solar cell (DSSCs) (a) Fe_2O_3 and (b) $BiFe_2O_3$ nanomaterial and (B) Coffee[b] leaf based extract (anthocyanins) dye based sensitized solar cell (DSSCs) (a) Fe_2O_3 and (b) $BiFe_2O_3$ nanomaterial

Dye sensitized solar cells (DSSCs)

DSSCs based on rosa flowers and coffee leaves extract: The prepared $BiFe_2O_3$ was also applied to make a standard solar cell based on rosa flower extract, which gives the high electroefficiency from short-circuit current density as compared to Fe_2O_3 as indicated from the results that rosa flowers based extract $BiFe_2O_3$ produce J_{sc} value of 8 mA/cm^2, whereas Fe_2O_3 produce J_{sc} value of 7.1 mA/cm^2. Similarly, using coffee leaf extract based dye sensitized solar cell (DSSCs), $BiFe_2O_3$ produce J_{sc} value of 6.4 mA/cm^2, while Fe_2O_3 produce J_{sc} value of 5.5 mA/cm^2 (Fig. 11).

Antibacterial activity: The disc diffusion method was used in this investigation to evaluate the Fe_2O_3 and $BiFe_2O_3$ nanomaterial's antibacterial efficacy against human bacterial pathogens (*Staphylococcus aureus* and *Escherichia coli*). The antibacterial activity results of undoped Fe_2O_3 and doped $BiFe_2O_3$ nanomaterials is shown in Fig. 12. The undoped Fe_2O_3 and doped $BiFe_2O_3$ nanomaterials are active almost equally to the standard ciprofloxacin against Gram-positive and Gram-negative

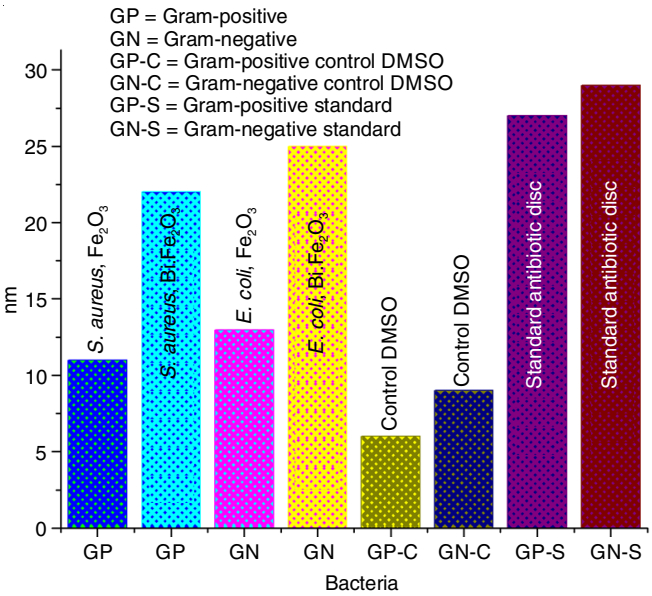

Fig. 12. Antibacterial activity [disc diffusion method]: (a) *Staphylococcus aureus* and (b) *Escherichia coli* investigation of prepared (a) Fe_2O_3 and (b) $BiFe_2O_3$ nanomaterial showed activity against both Gram-positive & Gram-negative strains

pathogenic organisms. Evaluation of $BiFe_2O_3$ nanomaterial as antibacterial agent is attributed due to the high value of electron holes charge separation through low band gap energy, which causes a decrease in the charge recombination and results in the significant antibacterial activity [37].

Conclusion

A combined co-precipitation and sonicated method was used to synthesize $BiFe_2O_3$ nanomaterial successfully. The HR-SEM analysis revealed that $BiFe_2O_3$ has a well-defined nanospherical like form. The produced spherical-like structure of the $BiFe_2O_3$ nanomaterial shows the strong photocatalytic activity when compared to Fe_2O_3 as confirmed through photoluminescence studies. The UV-Vis DRS results releaved the low band gap energy, making it useful as photocatalyst material for the degradation of rhodamine 6G and rhodamine B dyes. The generated nanomaterial was found to be stable and reusable after a feasible five time process. Furthermore, $BiFe_2O_3$ nanomaterial also exhibited the similar antibacterial activity towards *Escherichia coli* and *Staphylococcus aureus* bacterial pathogens as compared to standard ciprofloxacin.

CONFLICT OF INTEREST

The authors declare that there is no conflict of interests regarding the publication of this article.

REFERENCES

1. G. Catalan and J.F. Scott, *Adv. Mater.*, **21**, 2463 (2009); https://doi.org/10.1002/adma.200802849
2. H. Wu, J. Zhou, L. Liang, L. Li and X. Zhu, *J. Nanomater.*, **2014**, 471485 (2014); https://doi.org/10.1155/2014/471485
3. E.A.R. Assirey, *Saudi Pharm. J.*, **27**, 817 (2019); https://doi.org/10.1016/j.jsps.2019.05.003
4. M. Irshad, Q. Ain, M. Zaman, M.Z. Aslam, N. Kousar, M. Rafique, M. Asim, K. Siraj, A.N. Tabish, M. Usman, M.H. Farooq, M.A. Assiri and M. Imran, *RSC Adv.*, **12**, 7009 (2022); https://doi.org/10.1039/D1RA08185C
5. S. Irfan, Z. Zhuanghao, F. Li, Y.-X. Chen, G.-X. Liang, *J. Mater. Res. Technol.*, **8**, 6375 (2019); https://doi.org/10.1016/j.jmrt.2019.10.004
6. S. Gulati, K. Goyal, A. Arora, S. Kumar, M. Trivedi and S. Jain, *Environ. Sci. Water Res. Technol.*, **8**, 1590 (2022); https://doi.org/10.1039/D2EW00027J
7. A. Haruna, I. Abdulkadir and S.O. Idris, *Heliyon*, **6**, e03237 (2020); https://doi.org/10.1016/j.heliyon.2020.e03237

8. N. Boinis and H.B. Sharma, *Integr. Ferroelectr.*, **194**, 28 (2018); https://doi.org/10.1080/10584587.2018.1514858
9. S. Siebeneicher, F. Waag, M. Escobar-Castillo, V.V. Shvartsman, D.C. Lupascu and B. Gökce, *Nanomaterials*, **10**, 359 (2020); https://doi.org/10.3390/nano10020359
10. T.K. Pani, B. Sundaray, G. Sahoo and D. Rout, *J. Phys. D Appl. Phys.*, **53**, 325001 (2020); https://doi.org/10.1088/1361-6463/ab898f
11. N. Wang, X. Luo, L. Han, Z. Zhang, R. Zhang, H. Olin and Y. Yang, *Nano-Micro Lett.*, **12**, 81 (2020); https://doi.org/10.1007/s40820-020-00420-6
12. A.J. Preethi and M. Ragam, *J. Adv. Dielectr.*, **11**, 2130001 (2021); https://doi.org/10.1142/S2010135X21300012
13. J. Wu, Z. Fan, D. Xiao, J. Zhu and J. Wang, *Prog. Mater. Sci.*, **84**, 335 (2016); https://doi.org/10.1016/j.pmatsci.2016.09.001
14. Q. Zhang, D. Sando and V. Nagarajan, *J. Mater. Chem. C Mater. Opt. Electron. Devices*, **4**, 4092 (2016); https://doi.org/10.1039/C6TC00243A
15. Y. Mao, H. Zhou and S.S. Wong, *Mater. Matters*, **5.2**, 50 (2010).
16. G. Achenbach, W. James and R. Gerson, *J. Am. Ceram. Soc.*, **50**, 437 (1967); https://doi.org/10.1111/j.1151-2916.1967.tb15153.x
17. M. Muneeswaran, P. Jegatheesan and N. Giridharan, *J. Exp. Nanosci.*, **8**, 341 (2013); https://doi.org/10.1080/17458080.2012.685954
18. H. Xie, K. Wang, Y. Jiang, Y. Zhao and X. Wang, *Synth. React. Inorg. Met.-Org. Nano-Met. Chem.*, **44**, 1363 (2014); https://doi.org/10.1080/15533174.2013.801859
19. B. Liu, B. Hu and Z. Du, *Chem. Commun.*, **47**, 8166 (2011); https://doi.org/10.1039/c1cc11896j
20. S. Das and S. Basu, *J. Nanosci. Nanotechnol.*, **9**, 5622 (2009); https://doi.org/10.1166/jnn.2009.1152
21. L. Fang, J. Liu, S. Ju, F. Zheng, W. Dong and M. Shen, *Appl. Phys. Lett.*, **97**, 242501 (2010); https://doi.org/10.1063/1.3525573
22. N. Das, R. Majumdar, A. Sen and H.S. Maiti, *Mater. Lett.*, **61**, 2100 (2007); https://doi.org/10.1016/j.matlet.2006.08.026
23. T. Xian, H. Yang, X. Shen, J.L. Jiang, Z.Q. Wei and W.J. Feng, *J. Alloys Compd.*, **480**, 889 (2009); https://doi.org/10.1016/j.jallcom.2009.02.068
24. S. Ghosh, S. Dasgupta, A. Sen and H.S. Maiti, *Mater. Res. Bull.*, **40**, 2073 (2005); https://doi.org/10.1016/j.materresbull.2005.07.017
25. G. Dhir, P. Uniyal and N.K. Verma, *J. Magn. Magn. Mater.*, **394**, 372 (2015); https://doi.org/10.1016/j.jmmm.2015.07.002
26. J. Yang, X. Li, J. Zhou, Y. Tang, Y. Zhang and Y. Li, *J. Alloys Compd.*, **509**, 9271 (2011); https://doi.org/10.1016/j.jallcom.2011.07.023
27. X. Zheng, P. Chen, N. Ma, Z. Ma and D. Tang, *J. Mater. Sci. Mater. Electron.*, **23**, 990 (2012); https://doi.org/10.1007/s10854-011-0533-4
28. X. Wang, Y. Zhang and Z. Wu, *Mater. Lett.*, **64**, 486 (2010); https://doi.org/10.1016/j.matlet.2009.11.059
29. M. Popa, D. Crespo, J.M. Calderon-Moreno, S. Preda and V. Fruth, *J. Am. Ceram. Soc.*, **90**, 2723 (2007); https://doi.org/10.1111/j.1551-2916.2007.01779.x
30. I. Szafraniak, M. Polomska, B. Hilczer, A. Pietraszko and L. Kepinski, *J. Eur. Ceram. Soc.*, **27**, 4399 (2007); https://doi.org/10.1016/j.jeurceramsoc.2007.02.163
31. S. Rasalingam, H.S. Kibombo, C.M. Wu, R. Peng, J. Baltrusaitis and R.T. Koodali, *Appl. Catal. B*, **148-149**, 394 (2014); https://doi.org/10.1016/j.apcatb.2013.11.025
32. D. Raoufi and T. Raoufi, *Appl. Surf. Sci.*, **255**, 5812 (2009); https://doi.org/10.1016/j.apsusc.2009.01.010
33. S. Balachandran and M. Swaminathan, *Dalton Trans.*, **42**, 5338 (2013); https://doi.org/10.1039/c3dt33117b
34. S. Zinatloo-Ajabshir and M. Salavati-Niasari, *New J. Chem.*, **39**, 3948 (2015); https://doi.org/10.1039/C4NJ02106A
35. B. Krishnakumar, B. Subash and M. Swaminathan, *Sep. Purif. Technol.*, **85**, 35 (2012); https://doi.org/10.1016/j.seppur.2011.09.037
36. K. Ameta, P. Tak, D. Soni and S.C. Ameta, *Sci. Rev. Chem. Commun.*, **4**, 38 (2014).
37. K. Gupta, R.P. Singh, A. Pandey and A. Pandey, *Beilstein J. Nanotechnol.*, **4**, 345 (2013); https://doi.org/10.3762/bjnano.4.40